Co-doped hydroxyapatite as photothermal catalyst for selective CO_2 hydrogenation

Yong Peng [a], Horatiu Szalad [a], Pavle Nikacevic [b,c], Giulio Gorni [d], Sara Goberna [a], Laura Simonelli [d], Josep Albero [e,*], Núria López [b,*], Hermenegildo García [a,*]

[a] Instituto Universitario de Tecnología Química (CSIC-UPV), Universitat Politècnica de València, Avda. De los Naranjos s/n, Valencia 46022, Spain
[b] Institut Català d'Investigació Química (ICIQ), The Barcelona Institute of Science and Technology (BIST), Avda. Països Catalans 16, Tarragona 43007, Spain
[c] Universitat Rovira i Virgili (URV), Carrer de l'Escorxador s/n, Tarragona 43003, Spain
[d] ALBA Synchrotron Light Facility, Carrer de la Llum 2-26, Cerdanyola del Vallès 08290, Spain
[e] Departamento de Química/Instituto Universitario de Tecnología Química (CSIC-UPV), Universitat Politècnica de València, Camino de Vera s/n, 46022, Valencia (Spain)

ARTICLE INFO

ABSTRACT

The rational design and in deep understanding of efficient, affordable and stable materials to promote the light-assisted production of fuels and commodity chemicals is very appealing for energy crisis and climate change amelioration. Herein, we have prepared a series of Co-doped hydroxyapatite (HAP) catalysts with different Co content. The materials structure has been widely investigated by XRD, FT-IR, HRTEM, XPS, XAS, as well as computational simulations based on Density Functional Theory (DFT) with PBE functional. At low Co loading, there is a partial substitution of Ca cations in the HAP structure, while higher loadings promote the precipitation of small ($\sim$ 2 nm) Co nanoparticles on the HAP surface. For the optimal Co content, a constant CO rate of 62 mmol·g^{-1}·h^{-1} at 1 sun illumination and 400 °C, with the material being stable for 90 h. Visible and NIR photons have been determined responsible of the light-assisted activity enhanced. Mechanistic studies based on both experimental and DFT simulations show that H_2 preferentially adsorbs to metallic Co, while CO_2 adsorbs to the HAP surface oxygen. Moreover, both direct photo- and plasmon-driven contributions have been separated in order to study their mechanisms independently.

1. Introduction

Photocatalytic reduction of abundant resources, such as H_2O, N_2 or CO_2 has been proposed as an attractive approach for the environmentally friendly and sustainable production of high added-value fuels and chemicals.[1–5] Unlike other chemical processes, photocatalysis can directly utilize natural sunlight as a driving force to perform the chemical transformations without the need for prior light-to-electricity conversion by means of photovoltaic devices or wind turbines [6–8].

Photochemical solar fuel production is currently limited by the low light-to-chemical efficiency and the fact that in semiconductor-based photocatalysts[9] light harvesting is usually limited to UV and visible blue light.[1] In the semiconducting photocatalyst, photons with energy equal to or greater than the semiconductor band gap are converted into electron/hole pairs, the bottlenecks being to increase the efficiency of charge separation and to slow down the recombination kinetics to give change for electron transfer with substrates adsorbed on the particle surface.

As an alternative mechanism to the classical photoinduced charge separation in semiconductors,[10,11] photons from the visible and near infrared (NIR) region can interact with metal nanoparticles supported on thermally insulating materials[12] by the localized metal surface plasmon resonance (LSPR). In this pathway, photon absorption increases the catalytic conversion rates at the metal nanoparticle by the localized heating due to thermalization of the photon energy and generation of "hot carriers" that influence the electronic structure of the species involved in the reaction.[13–15] For example, Feng et al. reported a plasmonic structure of porous silica needles containing Co nanoparticles.[16] This photocatalyst absorbs light over the entire solar spectrum and promotes efficient photothermal of CO_2 to CO and CH_4 with a conversion rate of 0.61 mol·g^{-1}·h^{-1} without external heating under 20 Suns of illumination. Alternatively, Guo et al. developed a

---

Cu-substituted hydroxyapatite (HAP) catalyst that exhibited very high activity in the reverse water gas shift (RWGS) reaction,[17] with a CO production rate of 0.9 mmol·g^{-1}·h^{-1} under 40 suns light irradiation and without external heating.

In fact, HAP ($Ca_{10}(PO_4)_6(OH)_2$) is a well-known structure that can be found in nature as minerals or in bones and animal teeth. These materials can be easily prepared in large-scale from abundant raw materials, [16] allowing a large number of partial cation substitutions due to their high stability and structural flexibility.[18] Thus, Ca ions can be partially replaced by various divalent cations, such as Sr^{2+}, Ba^{2+}, Zn^{2+}, Cu^{2+}, or Co^{2+}. Moreover, they are thermally isolating materials, which make HAP very promising candidates as photothermal catalysts.

Herein, we have prepared a series of Co-doped HAP photocatalysts with increasing Co content for the selective gas-phase continuous flow CO_2 hydrogenation. CoHAP is a highly active and CO-selective photothermal CO_2 hydrogenation catalyst when exposed to 1 sun and controlled external heating. Mechanistically, we have isolated both direct photo- and plasmon-driven mechanisms in order to study them separately. Moreover, it has been revealed that the mechanisms occur depending on the Co doping level, reaching a maximum CO rate of 62 mmol·g^{-1}·h^{-1} at 1 sun illumination and 400 °C, with the material being stable for 90 h operation under continuous flow. These results pave the way for the design of efficient, affordable and stable materials to promote the light-assisted production of fuels and commodity chemicals.

2. Experimental section

2.1. Materials preparation

The synthesis of Co_xHAP catalysts followed a coprecipitation route as previously reported.[17] In a general procedure, the $Ca(NO_3)_2$ and $Co(NO_3)_2$ salts, with a Co to Ca atomic ratio equal to x% were solubilized in 100 mL of Milli-Q water. The pH of this solution was then adjusted to 10–11 by dropwise addition of an ammonium hydroxide solution. Then, 100 mL of a previously prepared phosphate solution (0.4 wt%) containing a stoichiometric amount of phosphate with respect to the total cations was added dropwise with vigorous stirring. The resulting suspension was then heated to 90 °C and stirred continuously for another 2 h, after which both heating and stirring were stopped. The solid was aged overnight, filtered, and dried in an electric oven at 100 °C. The prepared solid was then ground to a fine powder and calcined at 500 °C for 5 h at a heating rate of 2 °C/min, unless otherwise specified.

2.2. Characterization

Powder X-ray diffraction (PXRD) patterns were recorded on a Shimadzu XRD-7000 diffractometer by using Cu κ_α radiation ($\lambda = 1.5418$ Å), operating at 40 kV and 40 mA at a scan rate of 10° per min in the 2–90° 2θ range. Transmission electron microscopy (TEM) images were obtained using a Philips CM300 FEG microscope operating at 200 kV, coupled with an X-Max 80 energy dispersive X-ray (EDX) detector (Oxford instruments). The microscope is equipped with the STEM unit, the dark-field and high-angle field (HAADF) image detectors. The SEM images were collected with a JEOL JSM 6300 instrument equipped with an Oxford Instruments X-MAX detector. Co and Ca contents were determined by inductively coupled plasma-optical emission spectrophotometry (ICP-OES, Varian 715-ES, CA, USA). Diffuse reflectance UV/Vis spectra (DRS) in the 200–2000 nm range were collected in a Varian Cary 5000 spectrophotometer. X-ray photoelectron spectra (XPS) were measured on a SPECS spectrometer equipped with a Phoibos 150 MCD-9 detector using a nonmonochromatic X-ray source (Al) operating at 200 W. Samples for XPS were activated *in-situ* at 400 °C for 2 h in a prechamber under at 1×10^{-9} mbar prior to measurement. Fitting of the experimental data to individual components was calculated from the area of the corresponding peaks after nonlinear background subtraction of the Shirley type. Atomic ratios of the different elements were determined from the areas of the corresponding XPS peaks, corrected by the response factor of the spectrometer. The *in-situ* FTIR spectra were collected with a Bruker "Vertex 70″ and a Thermo Nicolet 8700 spectrophotometer equipped with a DTGS detector (4 cm^{-1} resolution, 32 scans). An IR cell allowing *in situ* treatments under controlled atmosphere and temperature from 25 to 500 °C was connected to a vacuum system with gas dosing device. Self-supporting pellets (approximately 10 mg cm^{-2}) were prepared from the sample powders by compaction and treated in a hydrogen stream (30 mL min^{-1}) at 400 °C for 2 h before testing. *In-situ* Raman spectra were obtained using a Renishaw "in Via" spectrophotometer equipped with an Olympus optical microscope. Samples were pretreated with H_2 at 400 °C for *in-situ* activation prior to spectrum collection. The H_2 desorption was monitored with a thermal conductivity detector (TCD) and a mass spectrometer following the characteristic mass of H_2 at 15 a.m.u. The CO_2 adsorption isotherms in the low-pressure range were measured in a Micromeritics ASAP 2010 instrument using ~200 mg of catalyst placed on a sample holder, which was then immersed in a liquid circulation thermostatic bath for precise temperature control. Prior to each measurement, the sample was treated overnight at 350 °C under vacuum and then measured at 0 °C.

The Co and Ca K-edge absorption spectra were collected at room temperature at the CLAESS beamline of the ALBA synchrotron.[19] The beam was monochromatized by means of a Si(111) double crystal monochromator, while the higher harmonics were rejected by choosing the correct angle and coating of the collimating and focusing mirrors. Data analysis was performed according to standard procedure using the Demeter XAS package[20]. The Fourier Transforms (FTs) of the Co and Ca K-edge EXAFS oscillations were extracted in the k-range of 2.43 − 9 Å^{-1} and the R-range between 1.3 and 23 Å with a Hanning window function. The available k ranges do not allow for modeling due to the correlations existing between the parameters. While quantification is not available, the data allow for a qualitative comparison as commented below.

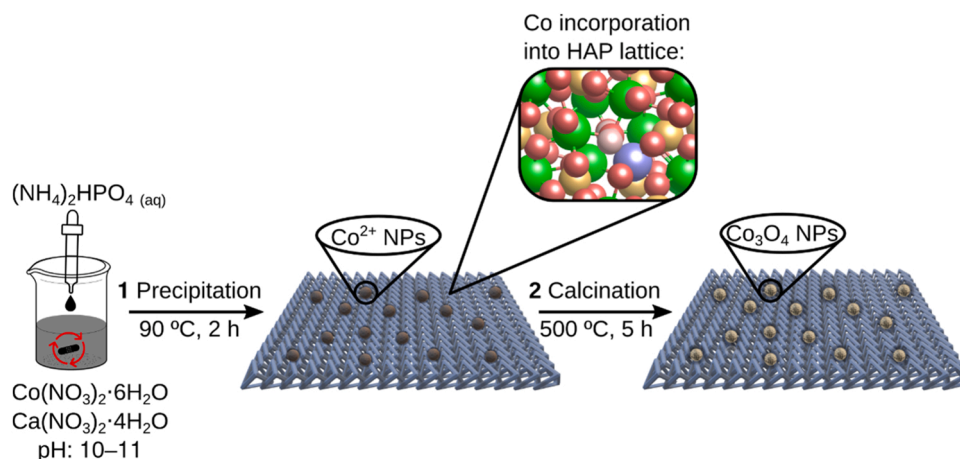### 2.3. Photo-assisted CO_2 hydrogenation

The photo-assisted CO_2 hydrogenation reactions were carried out in a customized glass flow reactor, as previously reported by our group. [21] Specifically, the reactor is wrapped with a heating ribbon and the temperature is controlled by a K-type thermocouple measuring the temperature of the catalyst surface. The catalyst surface is irradiated by a light beam introduced through a quartz optical fiber. In a typical test, 100 mg of catalyst was loaded onto the porous frit bed of the flow reactor and activated *in-situ* at 400 °C for 2 h. The feeding gas of CO_2 and H_2 was then introduced from the bottom of the reactor and flowed through the illuminated photocatalyst bed. The products were analyzed online using Varian gas chromatography (TCD detector and Carboxen®−1010 PLOT Capillary GC Column, L × I.D. 30 m × 0.53 mm, average thickness 30 μm).

3. Results and discussion

3.1. Materials preparation and characterization

Co-doped HAP (Co_xHAP) samples with different Co/Ca ratios (5, 10, 15 and 20 mol%) were prepared according to the synthetic procedure described in detail in the Experimental Section and illustrated in Scheme 1. For comparison purposes, HAP without Co was also prepared using an identical procedure. The final Co content in the Co_xHAP samples was determined by ICP-OES, resulting in a Co loading in Co_xHAP (x ∈ {5, 10, 15, 20}) of 3.46, 5.88, 8.75 and 11.38 wt%, respectively.

XRD patterns confirmed the successful formation of HAP with hexagonal structure (JCPDS No. 09–0432, Fig. S1 in Supporting Information). The experimental as well as the simulated (Fig. S2) XRD of Co_5HAP and $Co_{10}HAP$ show very similar patterns to HAP, although the diffraction peaks become broader, indicating lower crystallinity. Higher

Scheme 1. Co$_x$HAP preparation procedure including precursor precipitation (**1**) and subsequent calcination (**2**). Color code O: red, Co: purple, Ca: green, P: orange and H: white.

Co loadings, as in Co$_{15}$HAP and Co$_{20}$HAP samples, resulted in the disappearance of the HAP diffraction peaks (Fig. S1). These XRD data suggest that at low Co/Ca ratios, Co can be incorporated into the HAP structure with some distortion of the crystal lattice as a consequence of the ionic radius difference between Ca^{2+} and Co^{2+},[18] while further Co addition promotes phase segregation with a lack of crystallinity.

Despite the significant structural changes upon Co loading, the BET surface area and the average pore size of the Co$_x$HAP samples, determined by isothermal N$_2$ adsorption-desorption measurements, remain very similar (see Fig. S3 and Table S1). The large surface area values of these Co$_x$HAP samples are due to the reticular structure, as confirmed by HR-FESEM (Fig. S4). Furthermore, elemental mapping from a selected HR-FESEM image shows that Co is homogeneously distributed throughout the whole particle (Fig. S5).

Besides XRD, the changes in the HAP structure upon Co^{2+} loading can also be observed by Fourier-transformed infrared spectroscopy (FT–IR) (Fig. S6). The FT–IR spectrum of HAP shows the typical asymmetric stretching and bending modes of PO$_4^{3-}$ groups in the range of 951–1124 cm^{-1} and 529–611 cm^{-1}, respectively,[22] and the characteristic $^-$OH vibrational bands at ~3563 (ν_{OH}) and 630 cm^{-1} (δ_{OH}).[23] Upon Co^{+2} loading, the bands of both vibrational and bending modes of PO$_4^{3-}$ gradually become broader, reflecting the distortion of the PO$_4^{3-}$ configuration, probably due to the replacement of Ca^{2+} by Co^{2+} ions. In addition, the loss of the -OH signal and the appearance of an HPO$_4^{2-}$ band at ~2924 cm^{-1} suggest a cationic deficiency in the structure.

The catalyst structure was further investigated using computational simulations based on Density Functional Theory (DFT) with PBE functional.[24] Co-doped HAP was modeled as (0001) surface slab of HAP,
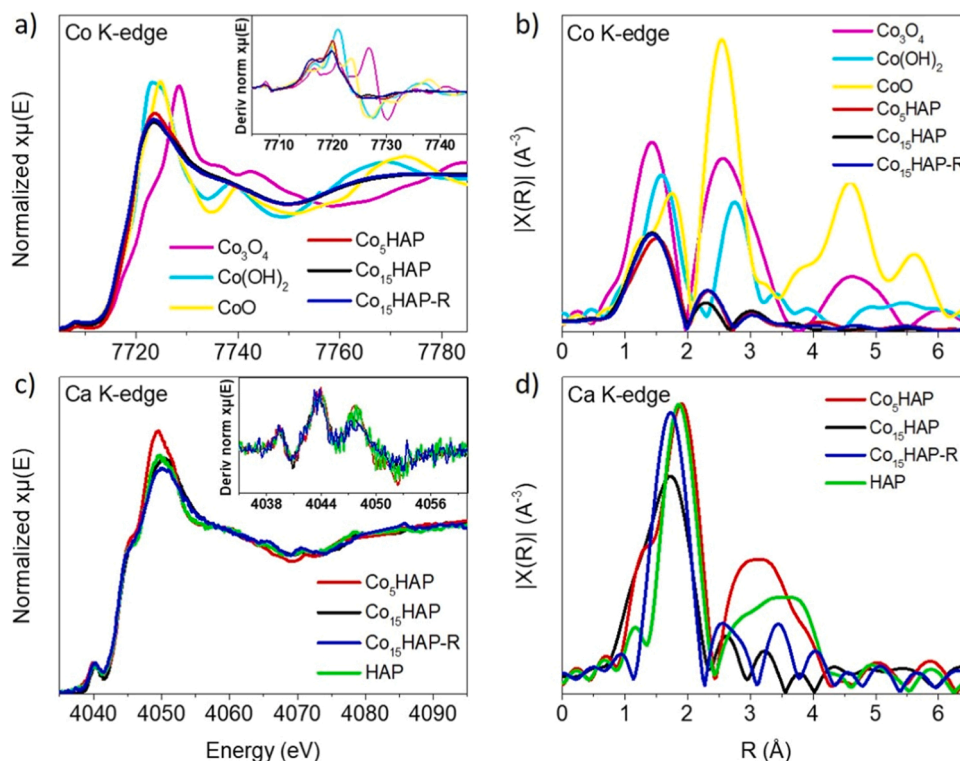

Fig. 1. XANES Co K-edge spectra (a) and their first derivatives (inset) as well as the corresponding Fourier transforms (b) of the different Co$_x$HAP samples studied. XANES Ca K-edge spectra (c) and their first derivatives (inset) as well as the corresponding Fourier transforms (d) of the different Co$_x$HAP samples studied.

[25,26] with one calcium atom substituted by cobalt (Fig. S7a). The doping site was determined to segregate toward the surface by comparing the relative energies of substitution of calcium ions by cobalt at different positions (Fig. S8). Metallic cobalt, as in the nanoparticles (*vide infra*) was modeled as the lowest-energy (0001) facet of hcp–Co (Fig. S7b). Optimized structures were in good agreement with the experimental measurements and were subsequently used to elucidate the reaction mechanism.

In order to further investigate the bulk structural characteristics in Co_xHAP samples, X-ray absorption spectroscopy (XAS) measurements were performed for CaHAP, Co_5HAP and $Co_{15}HAP$ (Fig. 1). The XANES Co K-edge spectra of Co_xHAP samples and Co^{2+} references (CoO, Co $(OH)_2$, Co_3O_4) and their corresponding first derivatives are shown in Fig. 1a. The common rising edge at around 7716 eV indicates a Co oxidation state close to 2 +, which is consistent with the most stable DFT-obtained magnetic moments for the Co atoms of 3 μ_B (high-spin d^7) and 1 μ_B (low-spin d^7).[16] However, some differences in the rising edges can be observed at higher energies due to the different Co local environment. The rising edge of $Co_{15}HAP$ samples is shifted to lower energy with respect to $Co(OH)_2$ and Co_3O_4 references, which is consistent with a lower oxidation state of Co or an elongated Co–O local bond. In addition, Co_5HAP shows a shift in spectral weight from lower (7716 eV) to higher (7721 eV) energies, indicating structural changes with increasing Co incorporation. The global Co K-edge XANES shape is compatible with the Co per Ca replacement due to its similarity to the Ca K-edge XANES shown in Fig. 1c. The slight increase in spectral weight around 7727 eV for the highest Co content could be compatible with the presence of Co_2O_3 impurities.

It is also worth noticing that the Co k-edge pre-peak intensity slightly decreases for the Co5HAP sample (see Fig. S9 a), in agreement with the expansion of the first shell (Fig. S9 c), which corresponds to a reduced hybridization between the Co 3d and the ligand p states. The filling of the gap between the Co K-edge pre-peak and the rising edge (around 7711 eV) after the reaction (green curve) could correspond to intra-site excitation, as reported earlier.[27] The Co k-edge pre-peak shifts toward higher energy in the Co5HAP is compatible with a different 3d levels configurations, which could depend from a change in the oxidation state, local magnetic moment, or local geometry. The shift of the rising edge inflection points toward higher energies (Fig. S9 b) could support a slight global increase in the cobalt oxidation state for the Co5HAP once compared with the Co15HAP sample.

The Fourier Transforms of the measured (Fig. 1b) and simulated (Fig. S10) EXAFS Co-K edge show a broad first shell peak (Co–O ~ 1.5 Å) and a strong damping of the more distant contributions. $Co_{15}HAP$ samples appear to have a contracted first shell (smaller Co–O distance). It is known from the literature that the replacement of Ca by ions with smaller ionic radius provokes a decrease in cell volume due to the smaller ionic radius and the more electronegative character of Co^{2+} compared to Ca^{2+},[18,28–30] while the incorporation of 3d-metal ions into the hexagonal channel of the apatite structure causes instead the expansion of the unit cell.[31,32] Therefore, the contraction of the Co–O first shell at low cobalt content in the structure suggests that when the content is low Co ions are incorporated into the hexagonal channel of the structure replacing some Ca positions, resulting in a unit cell contraction. The unit cell contraction of 1% (along the *b* direction) was also predicted by the DFT simulations (Table S2).

On the other hand, the FT signal corresponding to the second shell (Co–P ~ 2.3 Å) decreases in intensity with increasing the Co content in the calcined samples (from Co_5HAP to $Co_{15}HAP$), indicating a less ordered structure. This disorder increase correlates well with the observed broadening of the XRD peaks, indicating a decrease in crystallinity with increasing Co incorporation. The $Co_{15}HAP$ sample shows increased intensity on the FT second shell (Co-P ~ 2.3 Å) feature after the H_2 reduction, while the first shell signal remains unchanged. This suggests some sort of activation process that induces local ordering on the Co–P network.

The XANES Ca K-edge spectra of Co_xHAP samples (Fig. 1c) are similar to those of HAP, except that the energy position of the white line (at ~4050 eV) of samples with higher Co content ($Co_{15}HAP$) that shifts to higher energies with respect to the other samples, which may be indicative of local contraction. The pre-edge region at 4039.5 eV due to the 1 s → 3d electron transition, which is sensitive to the local distortion around calcium sites, is nearly identical regardless of Co content, suggesting that the local environment of Ca atoms is approximately the same in all Co_xHAP samples.

The Fourier Transforms of the measured and simulated EXAFS Ca-K edge spectra are shown in Fig. 1d and Fig. S9, respectively. For Co_5HAP, the first Ca–O shell (~ 1.8 Å) appears to be nearly coincident to that of HAP. However, the $Co_{15}HAP$ sample shows a contracted first shell (smaller R distance). It is clear that the first shells around both Ca and Co contract by increasing the amount of Co incorporated into the HAP lattice, probably due to a contraction of the lattice parameters as a consequence of a high degree of Ca^{2+}-by-Co^{2+} substitution. It is noteworthy that the intensity of the FT signals is significantly lower in the case of $Co_{15}HAP$. The decrease in intensity could reflect a loss of order around calcium due to structural distortions of the HAP lattice caused by the increasing Co incorporation. This effect agrees well with the XRD data, showing a loss of crystallinity at high Co content. Interestingly, for the $Co_{15}HAP$ system, the FT signal of the first shell increases significantly after reduction ($Co_{15}HAP$-R) indicating an increase in local structural order, consistent with increase in the structural order in the Co–P network detected at the Co K-edge (Fig. 1b).

The particle morphology of the Co_xHAP samples was studied in detail by HR-TEM (Fig. 2). The HR-TEM images show lattice fringes of 0.250 and 0.291 nm, corresponding to the interplanar spacing of the (301) and (211) facets of HAP. Interestingly, HR-TEM images of Co_xHAP samples revealed the presence of small and homogeneously distributed nanoparticles in the case of $Co_{10}HAP$, $Co_{15}HAP$ and $Co_{20}HAP$ samples. The concentration and size of these nanoparticles increased with the Co content, resulting in values of 1.0 ± 0.3, 1.3 ± 0.3 and 1.8 ± 0.5 nm for $Co_{10}HAP$, $Co_{15}HAP$ and $Co_{20}HAP$, respectively, after measurement of a statistically relevant number of these nanoparticles. According to previous XAS characterization these nanoparticles correspond to Co oxides formed by the excess of Co that does not become incorporated into the HAP lattice.

However, we were not able to identify the surface Co based NPs by EDX mapping that shows a homogenous distribution of all the elements (Fig. 2 n-r). This EDX information is compatible with the main proportion of Co element being incorporated in the HPA lattice together with Ca, and thus results in an overall homogenous distribution of Co and Ca elements. Changes in the crystallinity upon Co loading increase reported by XRD can also be observed in electron microscopy. Specifically, CaHAP shows very high crystallinity with a few grain boundaries, but the crystalline degree decreases with the Co content. Especially, amorphous phase appears in the case of Co_5HAP (red arrow mark in Fig. 2d), and a more obvious mixture of crystalline and amorphous areas can be observed in Fig. 2f ($Co_{10}HAP$), which is consistent with the decrease in peak intensity and broadening of peak width in XRD. This in the amorphous phase domains as the Co loading increases is reflected in the case of $Co_{15}HAP$ and $Co_{20}HAP$. Therefore, the lack of long-range crystallinity can be the explanation for the amorphous character of $Co_{15}HAP$ and $Co_{20}HAP$ samples.

The diffuse reflectance UV–vis–NIR absorption spectra of the Co_x-HAP samples were recorded. They are shown in Fig. S11. As can be seen there, pristine HAP shows negligible absorption in the visible and NIR regions, which is consistent with its large band gap as also estimated by *GW* approximation-based simulations (band gap of 6 eV for the (0001) surface slab of HAP; Fig. S12a). In comparison, the simulations indicate that Co_xHAP should exhibit several additional states within the band gap (Fig. S12b),[33] allowing for specific electronic transitions. There are five new states (both occupied and empty) localized within 2 eV from the valence band maximum. In fact, Co_5HAP shows a continuous
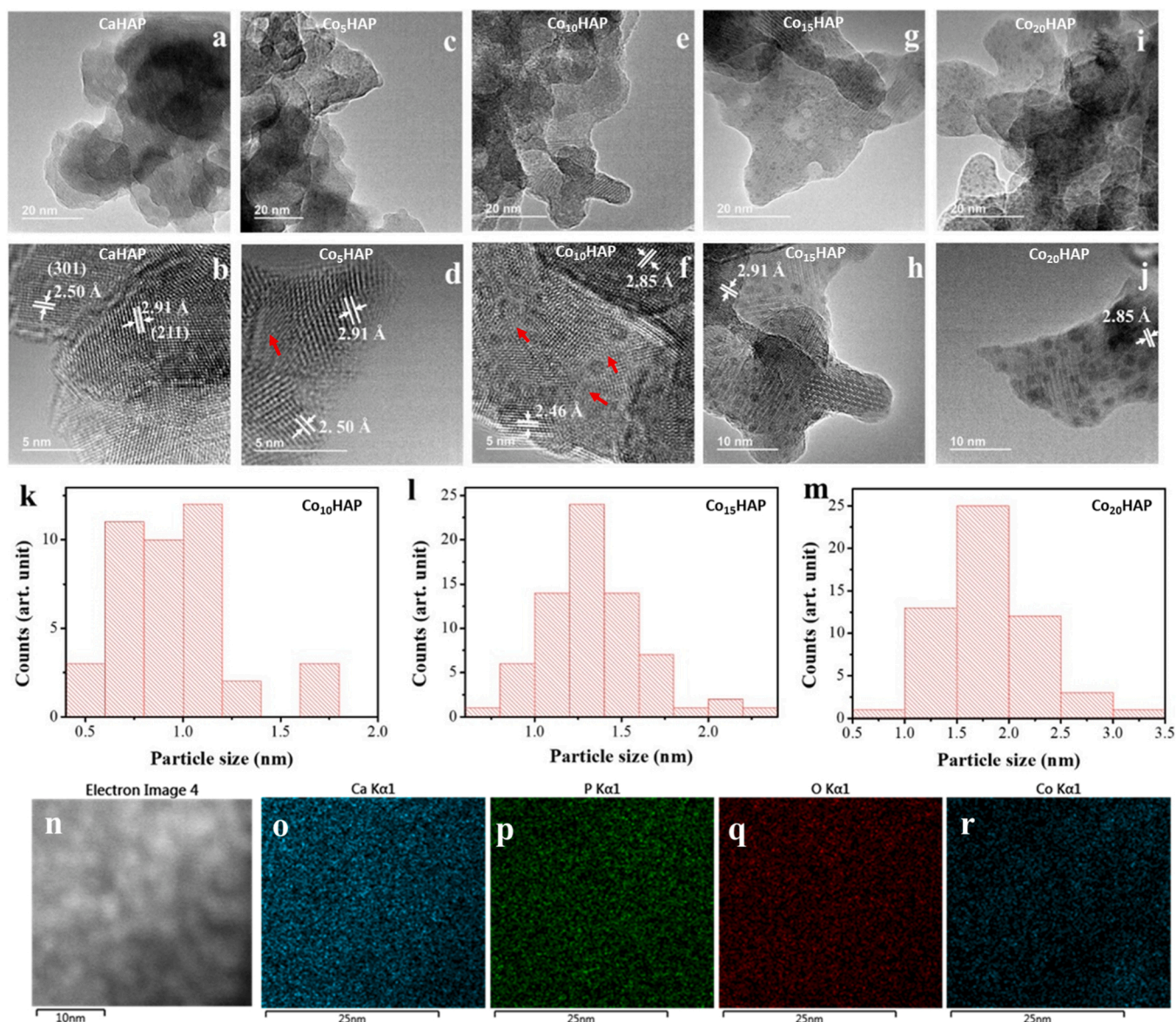
Fig. 2. HRTEM images of CaHAP (a and b), Co_5HAP (c and d), $Co_{10}HAP$ (e and f), $Co_{15}HAP$ (g and h) and $Co_{20}HAP$ (i and j). (Red arrows points to the amorphous area). The histograms of nanoparticle size distribution in $Co_{10}HAP$ (k), $Co_{15}HAP$ (l) and $Co_{20}HAP$ (m) are also shown. Images from n to r are the EDX mapping of $Co_{15}HAP$ sample.

absorption decreasing in intensity from the UV towards the NIR zone, and a broad and low intensity band in the region from 1000 to 1800 nm with relative maxima at 1330 and 1500 nm. Interestingly, further increase in Co^{2+} content promotes a drastic change in the diffuse reflectance absorption spectra. A strong band in the visible region with three maxima at 518, 581 and 624 nm, together with two shoulders at about 412 and 748 nm were recorded in the absorption spectra of $Co_{10}HAP$, $Co_{15}HAP$ and $Co_{20}HAP$. In addition, the intensity of the visible and NIR bands increased with Co^{2+} content. The shoulders observed at 412 and 748 nm were attributed to surface-anchored band gap energy transitions in Co_3O_4, as reported previously,[34] while the main absorption feature in the visible region, centered at 581 nm, could be due to new transitions in HAP upon Co^{2+} substitution. It is worth noting that this absorption band, which lacks noticeable shoulders, can also be observed in Co_xHAP samples before calcination (Fig. S11b), suggesting that this absorption band originates from Co^{2+} ions in HAP structure, while calcination could promote the formation of Co_3O_4 nanoparticles from the Co^{2+} excess and migration from the HAP lattice in the sample surface.

Further confirmation of Co_3O_4 nanoparticle formation in the Co_xHAP

surface can be provided by XPS. The high-resolution XPS Co 2p spectrum of $Co_{15}HAP$ and the best fit to individual components is shown in Fig. S13a. As can be seen there, the XPS Co 2p spectrum shows two major components at 782.2 eV and 798.0 eV, together with their corresponding satellite peaks at 785.8 and 803.3 eV assigned to Co^{2+}, and two minor components at 780.9 eV and 796.7 eV assigned to Co^{3+} species. [35–37] These data confirm the presence of Co_3O_4 in the Co_xHAP surface, in good agreement with the diffuse reflectance UV-Vis-NIR absorption and Raman spectroscopy experiments (*vide infra*).

Overall, the characterization data support the complete incorporation of Co^{2+} into the HAP lattice in Co_5HAP and the coexistence of Co^{2+} in the HAP and Co oxide nanoparticles, the latter increasing in density as the Co loading in the material increases. Sample activation causes a partial migration of Co^{2+} from the HAP structure to extra-framework positions.

3.2. Photo-assisted CO_2 hydrogenation

Photo-assisted CO_2 hydrogenation reactions were carried out in

continuous flow using a customized glass reactor with a thin circular (2.5 cm diameter) photocatalyst bed deposited on a porous quartz frit through which the gas flows from the bottom. The photocatalyst is illuminated from above by a quartz optical fiber inserted into the reactor (see Fig. S14 for details of the reaction setup and conditions). The temperature of the photocatalyst bed was measured under illumination and equilibrated to the desired value prior to photocatalytic hydrogenation. Irradiation was performed using the collimated output beam of a 150 W Xe lamp at 1080 W·m^{-2}, which resulted in a steady temperature of 156 °C without any external heating. Higher temperatures were achieved using an electric heater controlled by a thermocouple placed on the photocatalyst bed.

Prior to starting the photocatalytic reactions, the Co_xHAP samples were activated *in situ* in the reactor at 400 °C for 2 h in H_2 flow. This temperature was chosen based on the thermo-programmed reduction (TPR) data shown in Fig. S15. In these TPR measurements, Co_xHAP samples exhibit weak reduction peaks at temperatures below 400 °C, while more pronounced reduction peaks appear at temperatures between 600 and 700 °C. Since the maximum reaction temperature in this study is 400 °C, no significant structural changes in the samples are expected under reaction conditions after their prior activation.

To investigate the structural changes that occur during the activation step in $Co_{15}HAP$, *quasi-in situ* XPS studies were performed to determine the changes in the XPS Co spectra. The high-resolution XPS Co 2p spectrum of activated $Co_{15}HAP$ shows no components attributable to Co^{3+}, while typical components of Co^{2+} and Co^0 were recorded at 782.2 eV and 778.0 eV, respectively (Fig. S12a). These data would indicate a reduction of Co_3O_4 nanoparticles to Co^{2+} and metallic Co^0. Our DFT simulations for CoO show that its hydrogenation to metallic Co is extremely favorable with $\Delta G = -3.21$ eV, suggesting that the hydrogenation of Co_3O_4 should also be favorable. However, it is worth noting that the Co^{2+}/Co ratio at the $Co_{15}HAP$ surface is still as high as 3.4, indicating that the Co^{2+} species in the HAP lattice remain unchanged during the treatment. These results are in good agreement with the TPR data (Fig. S15), where the reduction peaks in $Co_{15}HAP$ below 400 °C (attributed to Co_3O_4 reduction) are much smaller than those at about 650 °C, which are attributed to the massive Co^{2+} reduction to

metallic Co. The high-resolution O 1 s spectra of activated and non-activated $Co_{15}HAP$ do provide a complementary information. They are shown in Fig. S13b. As can be observed there, the high-resolution XPS O 1 s spectrum of $Co_{15}HAP$ shows three main components centered at 528.8, 531.5 and 533.5 eV due to Co oxides (Co_3O_4), phosphate oxygen or hydroxide, and adsorbed water, respectively.[38,39] However, only one component at 531.3 eV can be observed upon activation, confirming the partial reduction of Co species. No changes in the XPS Ca 2p and P 2p spectra (Fig. S13c and d) indicate that the Co_xHAP structure was preserved upon activation. On the other hand, according to the diffuse reflectance UV–vis–NIR spectra, the visible absorption band derived from Co^{2+}-doping of HAP was preserved upon activation, while the features assigned to Co_3O_4 have disappeared after the activation process, in good agreement with the XPS results (Fig. S16).

Further evidence for the reduction of Co_3O_4 nanoparticles upon activation is provided by *in-situ* Raman experiments. Fig. S17 shows several Raman spectra of $Co_{15}HAP$ under H_2 flow at different temperatures. At room temperature, five Raman modes at 688, 617, 522, 479 and 192 cm^{-1} are observed, all of which are attributed to Co_3O_4, along with a weak peak at 955 cm^{-1} attributed to phosphate.[40,41] The vibrational peaks attributed to Co_3O_4 gradually disappear when the temperature reaches 300 °C, indicating Co_3O_4 reduction. On the contrary, the phosphate peak at 955 cm^{-1} remained unchanged during the *in-situ* H_2 treatment, demonstrating that the $Co_{15}HAP$ structure is preserved after activation.

The photocatalytic activity of Co_xHAP samples was first evaluated at 250 °C, either in the dark or under 1080 W/m^2 light irradiation. The results are summarized in Fig. 3a. As shown in Fig. 3a, the CO_2 conversion at 250 °C in the dark and after 1 sun irradiation using Co_5HAP was of 0.40% and 0.75%, respectively, with full (100%) selectivity toward CO. The small activity increase in light for the Co_5HAP system can be attributed to a photocatalytic enhancement of H_2 dissociation on Co-doped HAP *(vide infra)*. The CO_2 conversion increases with the Co loading up to a maximum conversion of 4.73% under 1 sun illumination, with CO selectivity above 99%, for $Co_{15}HAP$. However, only 1.1% conversion and 93% CO selectivity were achieved under dark conditions for this sample. HAP was also tested under dark and light conditions for
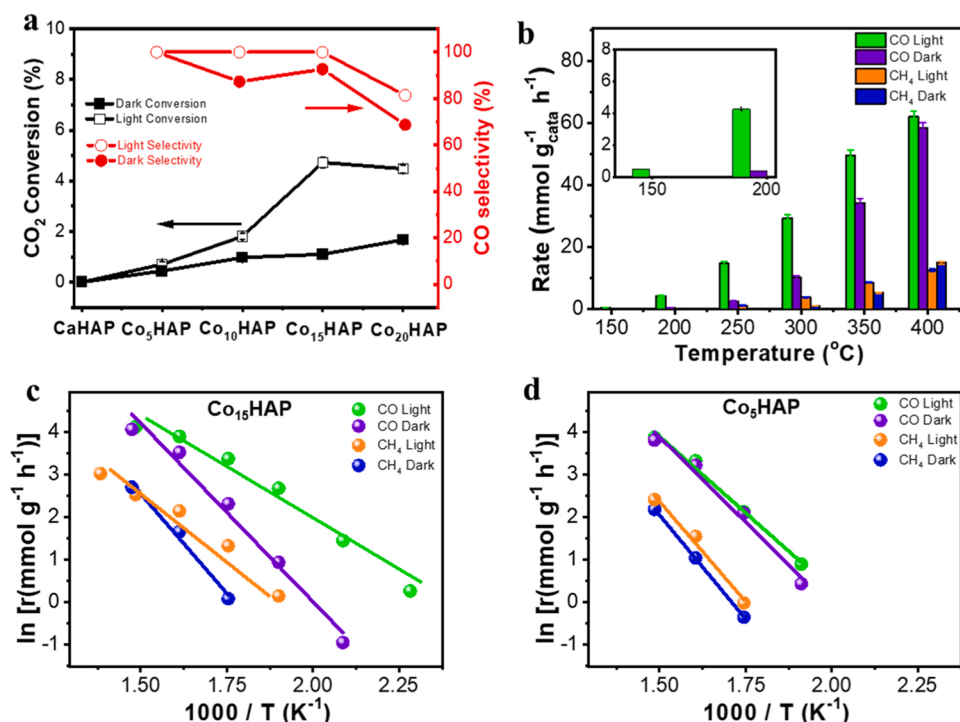

Fig. 3. (a) CO_2 conversion (black squares) and CO selectivity (red circles) of the samples studied at 250 °C under light illumination (empty circles and squares) and dark (filled circles and squares). (b) CO (green and purple columns) and CH_4 (orange and blue columns) production rates under light irradiation (green and orange) and dark (purple and blue) conditions, respectively, using $Co_{15}HAP$ at different temperatures. The inset shows magnification of the production rates at 156, 165 and 200 °C. Arrhenius plots of CO formation under light (green) and dark (purple) and CH_4 formation under light (orange) and dark (blue), respectively, obtained from the CO and CH_4 production rates at different temperatures using $Co_{15}HAP$ (c) and Co_5HAP (d). Reaction conditions: CO_2 13 mL/min + H_2 13 mL/min; 100 mg catalysts, 1080 W/m^2 light intensity.

CO_2 hydrogenation, but negligible amounts of CO or CH_4 were detected. Therefore, the Co species present in Co_xHAP appear to be responsible for the photocatalytic activity.

$Co_{15}HAP$ was then tested at different reaction temperatures, both under dark and one sun irradiation. As shown in Fig. 3**b**, CO evolution starts at 1080 $W \cdot m^{-2}$ light irradiation without external heating (T = 156 °C) and reaches 0.5 $mmol \cdot g^{-1} \cdot h^{-1}$ (0.14% CO_2 conversion). In the dark at 156 °C, CO levels were below the detectable limit, and even at 200 °C under dark conditions, the CO production rate obtained (0.1 $mmol \cdot g^{-1} \cdot h^{-1}$) was still lower than that under irradiation without external heating, indicating that light effectively assists the reaction. The CO production rate increased exponentially with temperature, reaching 62 mmol of $CO \cdot g^{-1} \cdot h^{-1}$ and 12.6 mmol of $CH_4 \cdot g^{-1} \cdot h^{-1}$ at 400 °C under one sun irradiation, corresponding to 17.8% CO_2 conversion. This CO_2 conversion is among the highest conversions in continuous flow operation at atmospheric pressure and light intensity of 1 sun using earth-abundant transition metal-based catalysts (see Table S3 for a comparison of the photocatalytic activity of $Co_{15}HAP$ with current state-of-the-art photocatalysts). It is worth noting that light irradiation resulted in an 11-fold increase in CO production under irradiation at 200 °C, while this factor decreases with temperature to ~1.2 at 400 °C. This trend can be rationalized by considering the operation of two different mechanisms. While the photocatalytic CO_2-based mechanism should predominate at low temperatures (< 250 °C) due to the negligible production rates of the purely thermo-catalytic mechanism at low temperatures, the thermo-catalytic CO production should dominate at higher temperatures, according to the Arrhenius theory. Additional experiments using isotopically labelled $^{13}CO_2$ were performed in order to rule out any carbon contamination as a source of the carbon products. The results are shown in Fig. S18. As can be seen there, only ^{13}CO was detected, confirming $^{13}CO_2$ as the main reagent and the presence of $^{13}CH_4$ was also confirmed.

Regarding the product distribution, it appears that small Co loadings favor CO selectivity, but an increase in Co content results in lower CO selectivity (up to ~70%), obtaining CH_4 as a co-product. The occurrence of an optimal Co loading could be justified by the occurrence of two opposing factors: (1) the increase in Co loading should lead to an increase in the number of active sites, resulting in higher activity, but (2) high Co loadings should also lead to larger average nanoparticle size and wider size distribution, as observed in Fig. 2, resulting in a decrease in photocatalytic activity.

The influence of temperature under light and dark conditions was further investigated. Arrhenius plots of CO and CH_4, under one sun and dark conditions, in $Co_{15}HAP$ and Co_5HAP are shown in Fig. 3**c** and **d**, respectively. The activation energies ($E_{a, app}$) for CO and CH_4 production under dark and light irradiation were calculated according to the Arrhenius equation and are summarized in Table S4. In all cases, the $E_{a, app}$ for CO formation is lower than that of CH_4, both under illuminated and dark conditions, in good agreement with the obtained production rates (Fig. 3b). On the other hand, the obtained $E_{a, app}$ for CO and CH_4 formation is higher for Co_5HAP than for $Co_{15}HAP$ under 1080 $W \cdot m^{-2}$ illumination, while $E_{a, app}$ values remain almost coincident in the dark. Furthermore, small differences in $E_{a, app}$ can be found for Co_5HAP under illuminated and dark conditions, while in the $Co_{15}HAP$ sample the $E_{a, app}$ under illumination is approximately half of the $E_{a, app}$ in the dark for both CO and CH_4. These results indicate a greater influence of light irradiation in $Co_{15}HAP$ than in Co_5HAP. The significant activity enhancement of light in the $Co_{15}HAP$ system can be attributed to the metallic Co nanoparticles absorbing light through the localized surface plasmon resonance (LSPR). This happens *via* two mechanisms: (1) hot carrier generation by intra/interband excitation and (2) local temperature increase.[42] The temperature increase was calculated according to ref. [43,44] and was found to be less than 1 μK. This leaves the plasmon-induced hot electron activation as the main contribution to the increased activity under illumination.

We were also interested in investigating which frequencies of the electromagnetic spectrum contribute to the photo-assisted CO_2 hydrogenation. To obtain this information, the CO production rate with $Co_{15}HAP$ and Co_5HAP was measured either with filtered light irradiation using different cut-off filters or in the dark, keeping constant the temperature at the catalyst bed at 250 °C. The results are shown in Fig. S19 **a** and **b**. As can be seen, both Co_xHAP samples behave similarly. UV light (λ < 380 nm) does not contribute significantly to the light-enhanced CO production, and the CO production rate is similar to that under dark conditions. Similarly, NIR light (λ > 830 nm) does not promote significant CO production enhancement upon irradiation. Therefore, the main contributor to the light-enhanced CO production rate appears to be the visible region. In fact, wavelengths below 455 nm only contribute a 8.9% of the total enhancement, while the remaining 90% of the light enhancement comes from the range of wavelengths between 455 and 750 nm. We have measured the UV–vis–NIR diffuse reflectance spectrum of activated $Co_{15}HAP$ ($Co_{15}HAP$-R) and compared it with the spectrum of the sample before activation (Fig. S16). As can be observed, the activated sample shows a narrower spectrum with a prominent band centered at 581 nm, but lacking the shoulders and the NIR band present in the $Co_{15}HAP$ sample before activation. These spectral changes may reflect the disappearance of the Co oxides detected in the sample prior to activation. Nevertheless, the absorption band between 450 and 750 nm in the visible region of the $Co_{15}HAP$-R spectrum is in perfect agreement with the photocatalytic activity as determined with filtered light illumination, indicating that this band in the visible region is uniquely responsible for the Co_xHAP photo-response.

3.3. Reaction mechanism

To gain additional insight into the reaction mechanism, *operando* Raman measurements were performed under reaction conditions. Fig. S20 shows the Raman spectra collected from the *in situ* activated $Co_{15}HAP$ sample under the reactant gas mixture (CO_2 at 10 $mL \cdot min^{-1}$ + H_2 at 10 $mL \cdot min^{-1}$) at 250 °C under light irradiation and dark conditions. It can be observed that several vibrational bands are present only under light irradiation. The peaks centered at 1581 and 1414 cm^{-1} can be assigned to polydentate/bidentate carbonate species,[45] while the bands at 1698 and 1834 cm^{-1} can be assigned to CO adsorbed on metallic Co (1735 cm^{-1} by DFT) and CO_2 adsorbed on HAP at a surface oxygen site (1855 cm^{-1} by DFT), respectively. The detected species suggest that the CO_2 is bound to the catalyst surface *via* *O, forming carbonate species, which are later probably reduced by hydrogen spillover from the Co nanoparticles, forming formate species, which finally decompose to CO (Fig. S21).[46] This is in agreement with the adsorption energies obtained by DFT simulations, which show that H_2 preferentially adsorbs to metallic Co, while CO_2 adsorbs to the HAP surface oxygen (Fig. 4). Additional bands at 680 and 610 cm^{-1} were assigned to Co_3O_4, indicating partial reoxidation of the metallic Co nanoparticles under the reaction conditions, which could be attributed to oxidation by CO_2 or the evolved H_2O product.

As noted above, the $E_{a, app}$ for $Co_{15}HAP$, obtained from the Arrhenius plot (Fig. 3c), show different values under illuminated and dark conditions, *i.e.*, they are lower under light illumination. These differences in $E_{a, app}$ indicate differences in the rate-determining step for this reaction under light irradiation and dark conditions. $E_{a, app}$ was derived from temperature measurements at the catalysts bed surface. Although it has been reported that the local temperature at the nanoscale on the active sites could be higher,[47] no direct evidences has been provided. Moreover, our theoretical simulations indicate a negligible change in the local temperature, and therefore it may be reasonable to draw conclusions based on these E_a values only.

Therefore, the partial reaction orders of H_2 and CO_2 under dark and light illumination were estimated for $Co_{15}HAP$ and Co_5HAP, since this parameter is measured at a constant temperature, and is generally independent of the reaction temperature. As shown in Fig. 5, the CO_2 reaction orders in $Co_{15}HAP$ under dark and light conditions were 0.55
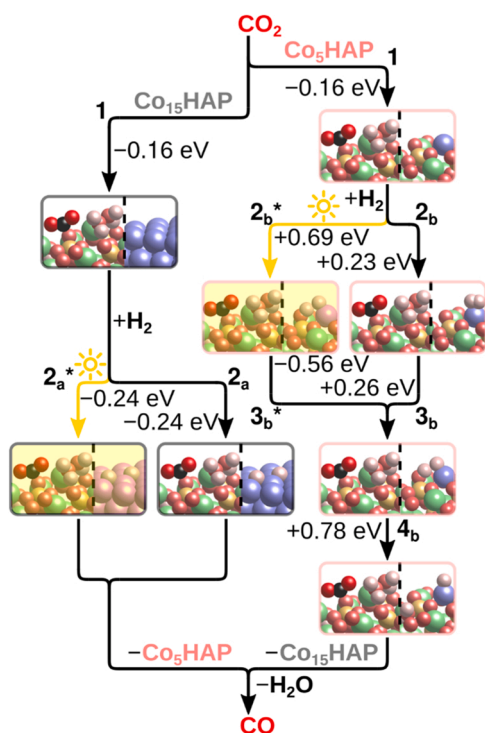
Fig. 4. CO_2 hydrogenation reaction pathway on $Co_{15}HAP$ (left) and Co_5HAP (right), with and without light, along with Gibbs free energy changes for selected processes. Visualized with VESTA.[48] Color code: Ca green; Co (ground state) blue; Co (excited state) pink; P yellow; O red; H white.

and 0.64, respectively. These values are similar, indicating no significant effect of light on CO_2 activation. Similarly, Co_5HAP presents CO_2 reaction order values under dark and light conditions of 1.15 and 1.09, respectively. The DFT simulations show that CO_2 binds to HAP ($\Delta G = -0.16$ eV; step **1** in Fig. 4) rather than to Co nanoparticles ($\Delta G =$

+1.15 eV; Table S5), and preferentially to the pristine material than to the Co-doped material ($\Delta G = +0.54$ eV for the Co-doped HAP; Table S5). This implies that in the real system, CO_2 tends to adsorb on the HAP surface oxygen atoms far from the Co site, so that the adsorbed CO_2 and the reaction intermediates derived from it are not directly affected by the photoexcitation. On the contrary, the H_2 reaction order in $Co_{15}HAP$ changes from 0.13 to -0.51 with illumination, while the values obtained for Co_5HAP do not change much (0.31 and 0.10 in dark and light, respectively). This is consistent with the fact that H_2 preferentially adsorbs on metallic Co ($\Delta G = -0.24$ eV; step **2$_a$**) rather than on Co-doped HAP ($\Delta G = +0.23$ eV; step **2$_b$**) and is thus affected by the LSPR induced by light on metallic Co in the $Co_{15}HAP$ system. The more exergonic and dissociative adsorption of H_2 on metallic Co also rationalizes the higher CO_2 hydrogenation activity on $Co_{15}HAP$ compared to Co_5HAP. The negative reaction order measured for $Co_{15}HAP$ can be understood as dissociative H_2 adsorption competing with CO_2 adsorption and decreasing the reaction rate.

In addition, an estimate of the CO_2 and H_2 reaction orders of the Co nanoparticles can be obtained by subtracting the values obtained from $Co_{15}HAP$ from those the ones obtained from Co_5HAP. As can be seen in Fig. S22, the CO_2 reaction order remained very similar in light and dark conditions with values close to 1, while the H_2 reaction order was negative in both dark and light conditions. This indicates that the H_2 dissociatively adsorbed on the Co nanoparticles spills over to all the sites and competes with CO_2 adsorption and activation.

The tendency of CO_2 and H_2 to adsorb to different sites in both Co_5HAP and $Co_{15}HAP$ keeps the adsorbed reactants spatially separated, but for the reaction to occur, they must clearly come close together. This can occur if the H_2 molecule dissociates and the individual proton atoms migrate to the CO_2 adsorption sites by hopping over oxygen atoms across the HAP surface. To investigate the feasibility of this process, the dissociation of H_2 on Co-doped HAP was modeled so that a single H atom leaves the Co site and adsorbs on a distant oxygen. In the dark, H_2 was first molecularly adsorbed (+0.23 eV; step **2$_b$**) and then partially dissociated (+0.26 eV; step **3$_b$**) by an H atom moving to one of the three nearby oxygen atoms in the form of a hydroxyl group. With light, H_2 is directly adsorbed in the partially dissociated state (step **2$_b$***) because it is
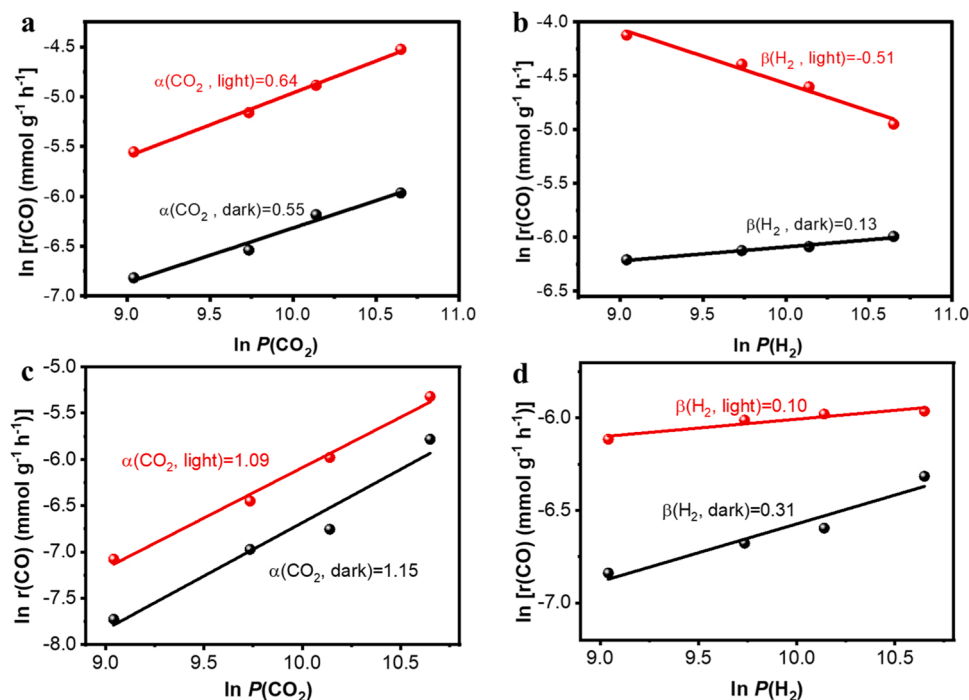

Fig. 5. Dependence of the CO production rate at 250 °C with the CO_2 partial pressure in dark (black) and light irradiation (red) (a and c) and H_2 partial pressure in dark (black) and light irradiation (red) (b and d) in $Co_{15}HAP$ (a and b) and Co_5HAP (c and d).

more stable than the molecularly adsorbed state (Table S6), indicating that irradiation facilitates H_2 dissociation. This result illustrates the photocatalytic potential of Co-doped HAP.

After the formation of the partially dissociated state, ΔG for further (complete) dissociation was found to be $+$ 0.78 eV (step **4b**), which is a rather high barrier. However, this barrier does not take into account the configurational entropy of the dissociated state which consists of many possible microstates, since there are many surface oxygens to which the hydrogen can jump. The high dissociation entropy would make the process feasible at the temperatures at which the reaction is performed. It is important to note that while the entropic effects promote H_2 dissociation, they also tend to make H_2 and CO_2 adsorption less favorable.

Having justified the transfer of protons between different sites, the transfer of electrons between the sites still remains to be explained. The intragap states introduced by the Co doping of HAP (Fig. S11) allow an enhanced electron transfer, especially during photoexcitation. In the case of $Co_{15}HAP$, photoexcitation allows for improved hot-electron transfer from the Co nanoparticle to the HAP phase by LSPR.[49] Another way to improve light absorption and charge transfer in a semiconductor is through oxygen vacancy formation,[50] which can be facilitated by doping with transition metals.[51] Our simulations show that the Gibbs energy required to form the oxygen vacancy by the oxidation of H_2 to H_2O in Co-doped HAP is 1.1 eV, compared to 2.1 eV for the pristine HAP.

Another point to note is that the calculated energies of CO_2 adsorption on HAP refer to the systems where H_2O is adsorbed on the surface metal atom (left undercoordinated by the surface cleavage), as seen in Fig. 4. In the absence of water molecules, the adsorption is ~1 eV less favorable (in both pristine and Co-doped HAP), even though the adsorbed CO_2 does not directly interact with H_2O or the metal on which H_2O is adsorbed. This is feasible in the real system, since water adsorption is favorable for HAP even at working temperatures ($\Delta G = -0.23$ eV; Table S5). On the other hand, H_2 does not adsorb on Co of Co-doped HAP when water already adsorbed. However, since the Gibbs free energy change of water adsorption on Co-doped HAP is not too low ($\Delta G = -0.26$ eV), a significant number of Co sites should be left uncoordinated by water, allowing H_2 adsorption. All the computed structures can be obtained in ref. [52].

3.4. Stability

The stability of $Co_{15}HAP$ as a selective photocatalyst for CO_2 hydrogenation was evaluated by performing the CO_2 hydrogenation reaction continuously for 90 h at the highest temperature (400 °C) under light irradiation. As shown in Fig. S23, $Co_{15}HAP$ exhibited high stability under these conditions, with only a 5% activity decrease in the CO formation rate after 90 h of reaction (from 73 mmol·g^{-1}·h^{-1} to 69.3 mmol·g^{-1}·h^{-1}). The XRD pattern of $Co_{15}HAP$ after continuous reaction for 90 h at 400 °C shows the same amorphous structure, with no evidence of agglomerated Co species (Fig. S24). The high dispersity and size of Co nanoparticles in $Co_{15}HAP$ after 90 h reaction was also confirmed by HR-TEM images (Fig. S25). The high stability of the supported nanoparticles could be attributed to a strong interaction with the support as a consequence of their growth from metal excess from the lattice upon thermal treatment, as reported previously.[53] Moreover, the porous structure, morphology and surface composition of $Co_{15}HAP$ remained unchanged as evidenced by HR-FESEM images (Fig. S26) and XPS measurements (Fig. S27).

These results are particularly interesting for potential industrial applications. The characterization after 90 h of reaction at the highest temperature does not suggest any structural or morphological changes, and therefore, it can assumed that this material could work continuously for even longer period, especially using lower temperatures.

4. Conclusion

It has been shown that the combination of framework and non-framework Co atoms in the hydroxyapatite structure renders a photocatalyst efficient to promote the light-assisted reverse water gas shift with a very high CO selectivity, which depends on the Co loading of the photocatalyst and the operating conditions. Sample characterization after the reductive H_2 activation pretreatment shows that the fine cobalt oxide nanoparticles present in Co_xHAP samples at Co loading > 5% are converted to metallic cobalt, while a significant percentage of Co^{+2} remains in the hydroxyapatite framework positions. The most active sample, $Co_{15}HAP$, is able to achieve 21.4% conversion under continuous flow and one sun illumination at 400 °C, which compares favorably with previously reported photocatalysts. At 300 °C and ambient pressure, CO formation rates up to 30 mmol$_{CO}$ g$_{catalyst}^{-1}$h^{-1} are achieved under one sun illumination, which is more than a 3-fold increase compared to the same process in the dark. The photocatalytic activity results from light absorption in the visible region and has been correlated with the presence of Co in the samples. The $Co_{15}HAP$ photocatalyst is remarkably stable, with only a 5% decrease in the CO formation rate after 90 h of operation and no observable changes in the physicochemical properties of the material. On the way to industrial application of photocatalytic processes, especially for solar fuels production, the present results show that it is possible to operate photocatalytic processes under continuous flow with high CO_2 conversions and remarkable photocatalytic activity at moderate temperatures.

CRediT authorship contribution statement

Yong Peng and Horatiu Szalad prepared the materials and performed the photocatalytic tests, Pavle Nikacevic and Núria López performed the theoretical calculations. Giulio Gorni, Sara Goberna and Laura Simonelli performed the XAS measurement and interpreted the results. Josep Albero and Hermenegildo García designed the research. The draft was written by Josep Albero and revised with the contribution of all authors.

Declaration of Competing Interest

The authors declare that they have no known competing financial interests or personal relationships that could have appeared to influence the work reported in this paper.

Data Availability

Data will be made available on request.

Acknowledgements

generaous computational resources.

Appendix A. Supporting information

Supplementary data associated with this article can be found in the online version at doi:10.1016/j.apcatb.2023.122790.

References

[1] E. Gong, S. Ali, C.B. Hiragond, H.S. Kim, N.S. Powar, D. Kim, H. Kim, S.-I. In, Solar fuels: research and development strategies to accelerate photocatalytic CO₂ conversion into hydrocarbon fuels, Energy Environ. Sci. 15 (2022) 880–937.

[2] J. Yu, T. Zhang, N. Wu, Solar photocatalysis, Sol. RRL 5 (2021), 2100037.

[3] A. Galushchinskiy, R. González-Gómez, K. McCarthy, P. Farràs, A. Savateev, Progress in development of photocatalytic processes for synthesis of fuels and organic compounds under outdoor solar light, Energy Fuels 36 (2022) 4625–4639.

[4] Y.-H. Chen, M.-Y. Qi, Y.-H. Li, Z.-R. Tang, T. Wang, J. Gong, Y.-J. Xu, Activating two-dimensional Ti3C2Tx-MXene with single-atom cobalt for efficient CO₂ photoreduction, Cell Rep. 2 (2021), 100371.

[5] S.-H. Li, M.-Y. Qi, Y.-Y. Fan, Y. Yang, M. Anpo, Y.M.A. Yamada, Z.-R. Tang, Y.-J. Xu, Modulating photon harvesting through dynamic non-covalent interactions for enhanced photochemical CO₂ reduction, Appl. Catal. 292 (2021), 120157.

[6] N.S. Lewis, Research opportunities to advance solar energy utilization, Science 351 (2016) 1920.

[7] F. Zhang, Y.-H. Li, M.-Y. Qi, Z.-R. Tang, Y.-J. Xu, Boosting the activity and stability of Ag-Cu₂O/ZnO nanorods for photocatalytic CO₂ reduction, Appl. Catal. 268 (2020), 118380.

[8] H.-K. Wu, Y.-H. Li, M.-Y. Qi, Q. Lin, Y.-J. Xu, Enhanced photocatalytic CO₂ reduction with suppressing H₂ evolution via Pt cocatalyst and surface SiO₂ coating, Appl. Catal. 278 (2020), 119267.

[9] T. Inoue, A. Fujishima, S. Konishi, K. Honda, Photoelectrocatalytic reduction of carbon dioxide in aqueous suspensions of semiconductor powders, Nature 277 (1979) 637–638.

[10] L. Yuan, M.-Y. Qi, Z.-R. Tang, Y.-J. Xu, Coupling strategy for CO₂ valorization integrated with organic synthesis by heterogeneous photocatalysis, Angew. Chem. Int. Ed. 60 (2021) 21150–21172.

[11] K.-Q. Lu, Y.-H. Li, F. Zhang, M.-Y. Qi, X. Chen, Z.-R. Tang, Y.M.A. Yamada, M. Anpo, M. Conte, Y.-J. Xu, Rationally designed transition metal hydroxide nanosheet arrays on graphene for artificial CO₂ reduction, Nat. Commun. 11 (2020) 5181.

[12] M. Ghoussoub, M. Xia, P.N. Duchesne, D. Segal, G. Ozin, Principles of photothermal gas-phase heterogeneous CO₂ catalysis, Energy Environ. Sci. 12 (2019) 1122–1142.

[13] F. Zhang, Y.-H. Li, M.-Y. Qi, Y.M.A. Yamada, M. Anpo, Z.-R. Tang, Y.-J. Xu, Photothermal catalytic CO₂ reduction over nanomaterials, Chem. Catal. 1 (2021) 272–297.

[14] Y. Peng, J. Albero, A. Franconetti, P. Concepción, H. García, Visible and NIR light assistance of the N₂ reduction to NH₃ catalyzed by Cs-promoted Ru nanoparticles supported on strontium titanate, ACS Catal. 12 (2022) 4938–4946.

[15] L. Wang, M. Ghoussoub, H. Wang, Y. Shao, W. Sun, A.A. Tountas, T.E. Wood, H. Li, J.Y.Y. Loh, Y. Dong, M. Xia, Y. Li, S. Wang, J. Jia, C. Qiu, C. Qian, N.P. Kherani, L. He, X. Zhang, G.A. Ozin, Photocatalytic hydrogenation of carbon dioxide with high selectivity to methanol at atmospheric pressure, Joule 2 (2018) 1369–1381.

[16] K. Feng, S. Wang, D. Zhang, L. Wang, Y. Yu, K. Feng, Z. Li, Z. Zhu, C. Li, M. Cai, Z. Wu, N. Kong, B. Yan, J. Zhong, X. Zhang, G.A. Ozin, L. He, Cobalt plasmonic superstructures enable almost 100% broadband photon efficient CO₂ photocatalysis, Adv. Mater. 32 (2020) 2000014.

[17] J. Guo, P.N. Duchesne, L. Wang, R. Song, M. Xia, U. Ulmer, W. Sun, Y. Dong, J.Y. Y. Loh, N.P. Kherani, J. Du, B. Zhu, W. Huang, S. Zhang, G.A. Ozin, High-performance, scalable, and low-cost copper hydroxyapatite for photothermal CO₂ reduction, ACS Catal. 10 (2020) 13668–13681.

[18] L. Veselinovic, L. Karanovic, Z. Stojanovic, I. Bracko, S. Markovic, N. Ignjatovic, D. Uskokovic, Crystal structure of cobalt-substituted calcium hydroxyapatite nanopowders prepared by hydrothermal processing, J. Appl. Crystallogr. 43 (2010) 320–327.

[19] L. Simonelli, C. Marini, W. Olszewski, M. Ávila Pérez, N. Ramanan, G. Guilera, V. Cuartero, K. Klementiev, CLÆSS: The hard X-ray absorption beamline of the ALBA CELLS synchrotron, Cogent Phys. 3 (2016), 1231987.

[20] B. Ravel, M. Newville, ATHENA, ARTEMIS, HEPHAESTUS: data analysis for X-ray absorption spectroscopy using IFEFFIT, J. Synchrotron Radiat. 12 (2005) 537–541.

[21] D. Mateo, J. Albero, H. García, Titanium-perovskite-supported RuO₂ nanoparticles for photocatalytic CO₂ methanation, Joule 3 (2019) 1949–1962.

[22] J. Gómez-Morales, C. Verdugo-Escamilla, R. Fernández-Penas, C.M. Parra-Milla, C. Drouet, F. Maube-Bosc, F. Oltolina, M. Prat, J.F. Fernández-Sánchez, Luminescent biomimetic citrate-coated europium-doped carbonated apatite nanoparticles for use in bioimaging: physico-chemistry and cytocompatibility, RSC Adv. 8 (2018) 2385–2397.

[23] K. Lin, Y. Zhou, Y. Zhou, H. Qu, F. Chen, Y. Zhu, J. Chang, Biomimetic hydroxyapatite porous microspheres with co-substituted essential trace elements: Surfactant-free hydrothermal synthesis, enhanced degradation and drug release, J. Mater. 21 (2011) 16558–16565.

[24] J.P. Perdew, K. Burke, M. Ernzerhof, Generalized gradient approximation made simple, Phys. Rev. Lett. 77 (1996) 3865–3868.

[25] H. Brasil, A.F.B. Bittencourt, K.E.S. Yokoo, P.C.D. Mendes, L.G. Verga, K. F. Andriani, R. Landers, J.L.F. Da Silva, G.P. Valença, Synthesis modification of hydroxyapatite surface for ethanol conversion: The role of the acidic/basic sites ratio, J. Catal. 404 (2021) 802–813.

[26] A. Slepko, A.A. Demkov, First principles study of hydroxyapatite surface, J. Chem. Phys. 139 (2013), 044714.

[27] L. Simonelli, E. Paris, C. Iwai, K. Miyoshi, J. Takeuchi, T. Mizokawa, N.L. Saini, High resolution x-ray absorption and emission spectroscopy of LixCoO₂ single crystals as a function delithiation, J. Phys.: Condens. Matter 29 (2017), 105702.

[28] H.R. Low, N. Phonthammachai, A. Maignan, G.A. Stewart, T.J. Bastow, L.L. Ma, T. J. White, The crystal chemistry of ferric oxyhydroxyapatite, Inorg 47 (2008) 11774–11782.

[29] T.J. White, D. ZhiLi, Structural derivation and crystal chemistry of apatites, Acta Cryst. B 59 (2003) 1–16.

[30] K. Zhu, K. Yanagisawa, R. Shimanouchi, A. Onda, K. Kajiyoshi, Preferential occupancy of metal ions in the hydroxyapatite solid solutions synthesized by hydrothermal method, J. Eur. Ceram. 26 (2006) 509–513.

[31] P.E. Kazin, O.R. Gazizova, A.S. Karpov, M. Jansen, Y.D. Tretyakov, Incorporation of 3d-metal ions in the hexagonal channels of the Sr₅(PO₄)₃OH apatite, Solid State Sci. 9 (2007) 82–87.

[32] T. Baikie, S.S. Pramana, C. Ferraris, Y. Huang, E. Kendrick, K.S. Knight, Z. Ahmad, T.J. White, Polysomatic apatites, Acta Cryst. B 66 (2010) 1–16.

[33] L. Hedin, New method for calculating the one-particle green's function with application to the electron-gas problem, Phys. Rev. 139 (1965) A796–A823.

[34] C. Ravi Dhas, R. Venkatesh, K. Jothivenkatachalam, A. Nithya, B. Suji Benjamin, A. Moses Ezhil Raj, K. Jeyadheepan, C. Sanjeeviraja, Visible light driven photocatalytic degradation of Rhodamine B and Direct Red using cobalt oxide nanoparticles, Ceram. Int. 41 (2015) 9301–9313.

[35] T.J. Chuang, C.R. Brundle, D.W. Rice, Interpretation of the x-ray photoemission spectra of cobalt oxides and cobalt oxide surfaces, Surf. Sci. 59 (1976) 413–429.

[36] Y. Bi, Z. Cai, D. Zhou, Y. Tian, Q. Zhang, Q. Zhang, Y. Kuang, Y. Li, X. Sun, X. Duan, Understanding the incorporating effect of Co²⁺/Co³⁺ in NiFe-layered double hydroxide for electrocatalytic oxygen evolution reaction, J. Catal. 358 (2018) 100–107.

[37] H. Liu, S. Cao, J. Zhang, S. Liu, C. Chen, Y. Zhang, S. Wei, Z. Wang, X. Lu, Facile control of surface reconstruction with Co²⁺ or Co³⁺-rich (oxy)hydroxide surface on ZnCo phosphate for large-current-density hydrogen evolution in alkali, Mater 20 (2021), 100448.

[38] D. Ressnig, M. Shalom, J. Patscheider, R. Moré, F. Evangelisti, M. Antonietti, G. R. Patzke, Photochemical and electrocatalytic water oxidation activity of cobalt carbodiimide, J. Mater. Chem. A 3 (2015) 5072–5082.

[39] R. Gresch, W. Müller-Warmuth, H. Dutz, X-ray photoelectron spectroscopy of sodium phosphate glasses, J. Non-Cryst. 34 (1979) 127–136.

[40] Y. Wang, X. Wei, X. Hu, W. Zhou, Y. Zhao, Effect of formic acid treatment on the structure and catalytic activity of Co₃O₄ for N₂O decomposition, Catal 149 (2019) 1026–1036.

[41] U. Anjaneyulu, D.K. Pattanayak, U. Vijayalakshmi, Snail shell derived natural hydroxyapatite: effects on NIH-3T3 cells for orthopedic applications, Mater. Manuf. Process. 31 (2016) 206–216.

[42] R.C. Elias, S. Linic, Elucidating the roles of local and nonlocal rate enhancement mechanisms in plasmonic catalysis, J. Am. Chem. Soc. 144 (2022) 19990–19998.

[43] G. Baffou, R. Quidant, F.J. García de Abajo, Nanoscale control of optical heating in complex plasmonic systems, ACS Nano 4 (2010) 709–716.

[44] G. Baffou, R. Quidant, Thermo-plasmonics: using metallic nanostructures as nano-sources of heat, Laser Photonics Rev. 7 (2013) 171–187.

[45] A. Efremova, T. Rajkumar, Á. Szamosvölgyi, A. Sápi, K. Baán, I. Szenti, J. Gómez-Pérez, G. Varga, J. Kiss, G. Halasi, Á. Kukovecz, Z. Kónya, Complexity of a Co₃O₄ system under ambient-pressure CO₂ methanation: influence of bulk and surface properties on the catalytic performance, J. Phys. Chem. C 125 (2021) 7130–7141.

[46] L. Liu, A.V. Puga, J. Cored, P. Concepción, H. García-Dieste, H. García, A. Corma, Sunlight-assisted hydrogenation of CO₂ into ethanol and C2+ hydrocarbons by sodium-promoted Co@C nanocomposites, Appl. Catal. 235 (2018) 186–196.

[47] R. Verma, R. Belgamwar, V. Polshettiwar, Plasmonic photocatalysis for CO₂ conversion to chemicals and fuels, ACS Mater. 3 (2021) 574–598.

[48] K. Momma, F. Izumi, VESTA: a three-dimensional visualization system for electronic and structural analysis, J. Appl. Crystallogr. 41 (2008) 653–658.

[49] A. Furube, S. Hashimoto, Insight into plasmonic hot-electron transfer and plasmon molecular drive: new dimensions in energy conversion and nanofabrication, NPG Asia Mater. 9 (2017) e454-e454.

[50] P. Nikačević, F.S. Hegner, J.R. Galán-Mascarós, N. López, Influence of oxygen vacancies and surface facets on water oxidation selectivity toward oxygen or hydrogen peroxide with BiVO₄, ACS Catal. 11 (2021) 13416–13422.

[51] B.-H. Lee, E. Gong, M. Kim, S. Park, H.R. Kim, J. Lee, E. Jung, C.W. Lee, J. Bok, Y. Jung, Y.S. Kim, K.-S. Lee, S.-P. Cho, J.-W. Jung, C.-H. Cho, S. Lebègue, K.T. Nam, H. Kim, S.-I. In, T. Hyeon, Electronic interaction between transition metal single-atoms and anatase TiO₂ boosts CO₂ photoreduction with H₂O, Energy Environ. Sci. 15 (2022) 601–609.

[52] https://iochem-bd.iciq.es/browse/review-collection/100/53695/ 51454418e7670d87acc8905d.

[53] M. Kothari, Y. Jeon, D.N. Miller, A.E. Pascui, J. Kilmartin, D. Wails, S. Ramos, A. Chadwick, J.T.S. Irvine, Platinum incorporation into titanate perovskites to deliver emergent active and stable platinum nanoparticles, Nat. Chem. 13 (2021) 677–682.